

# Inference Graphs for CNN Interpretation

Anonymous ECCV submission

Paper ID 4871

**Abstract.** Convolutional neural networks (CNNs) have achieved superior accuracy in many visual related tasks. However, the inference process through intermediate layers is opaque, making it difficult to interpret such networks or develop trust in their operation. We propose to model the network hidden layers activity using probabilistic models. The activity patterns in layers of interest are modeled as Gaussian mixture models, and transition probabilities between clusters in consecutive modeled layers are estimated. Based on maximum-likelihood considerations, a subset of the nodes and paths relevant for network prediction are chosen, connected, and visualized as an inference graph. We show that such graphs are useful for understanding the general inference process of a class, as well as explaining decisions the network makes regarding specific images. In addition, the models provide an interesting observation regarding the highly local nature of column activities in top CNN layers.

**Keywords:** Deep Neural Networks, Visualization, Interpretable AI

## 1 Introduction

Thanks to their impressive performance, convolutional neural networks (CNNs) are the leading architecture for tasks in computer vision [1,2,3]. However, due to their complex end-to-end training and architecture, understanding of their decision-making process and task assignment across hidden layers is lacking. This turns network interpretability into a difficult problem, and undermines usage of deep networks when high reliability and inference transparency are required. Understanding CNN reasoning by decomposing it into layer-wise stages can provide insights about cases of failure, and reveal weak spots in the network architecture, training scheme, or data-collection mechanism. In turn, these insights can lead to more robust networks and develop more trust in CNN decisions.

As we see it, enabling human understanding of the deep network inference process requires facing a main challenge of transforming CNN activities into discrete representations amendable to human reasoning. Deep networks operate through a series of distributed layer representations. Human language, however, is made up of discrete symbols, i.e., words, having meaning grounded by their reference in the world of objects, predicates, and their interrelations. The question of interest in this respect is: *Can we convert distributed representations into a human-oriented language?*, more technically, can we learn a dictionary of visual words and model their interrelationships leading to an interpretable inference graph?

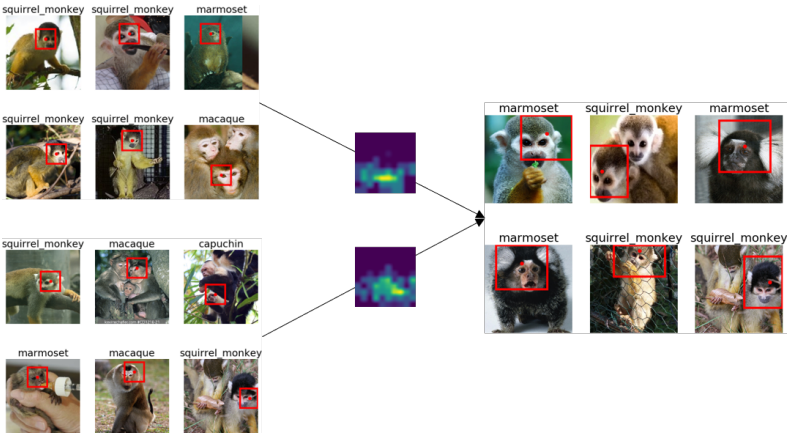


**Fig. 1. Visual words connected to form an inference path.** Two visual words in a lower network layer (left) (each is represented by six most typical images), representing the monkey eye (top) and face (bottom), explain a visual word in an upper network layer (right) that represents the monkey face. The heatmaps show spatial densities of lower-layer visual words in the receptive field of the higher-level word (see Section 4.3).

To address this, we suggest to describe the inference process of a network with probabilistic models. We model activity vectors in each layer as arising from a multivariate Gaussian mixture model (GMM). Layer activity in fully connected (FC) layers, or spatial location activity in convolutional layers, is associated with one of  $K$  clusters (GMM components), each representing a visual word. Connections between visual words of consecutive layers are modeled using conditional probabilities. For a multilayer perceptron (MLP) network, a full model with efficient inference can be obtained using a hidden Markov model (HMM). For the convolutional layers, each spatial location has its own hidden variable and dependencies among visual words in consecutive layers are described using conditional probability tables. Given a selected subset of images to be explained (either a specific image or images of an entire class), we describe the decision process of the network using an inference graph, representing the visual words used in different hidden layers and their probabilistic connections. As the full graph may contain thousands of visual words, a useful explanation has to find informative subgraphs, containing the most explanatory words w.r.t the network decision, and the likely paths connecting them. We suggest an algorithm for finding such graphs based on maximum-likelihood considerations.

Our contributions are: (i) a new approach for network interpretation, providing a formalism for probabilistic reasoning about inference processes in deep networks, and (ii) a graph-mining algorithm and visual tools enabling inference understanding. Our suggested inference graph provides a succinct summary of the inference process performed on a specific class of images or a single image, as inference progresses through the network layers. An example of visual nodes and the inferred connection between them is shown in Fig. 1.

## 090 2 Related Work

091 **Network visualization.** Several techniques have been suggested to visualize  
 092 network behavior. In activation maximization [4], the input that maximizes the  
 093 score of a given hidden unit is visualized by carrying out regularized gradient as-  
 094 cent optimization in the image space, as was applied to output class neurons [5]  
 095 and intermediate layer neurons [6]. Another technique [5] visualizes the gradient  
 096 strength in the original image space for a specific example, providing a "saliency  
 097 map" showing class score sensitivity to image pixels. The idea was extended to  
 098 an entire class of interest in [7]. In [8], the role of neurons in intermediate layers  
 099 was visualized by an inverse de-convolution network.  
 100

101 **Simplifying network representation.** Similar to our work, several works  
 102 looked for categorizing features through clustering [9,10]. Liao et al. [9] added  
 103 a regularization term encouraging the network representation to form three  
 104 kinds of clusters governed by examples, spatial locations, and channels. A simi-  
 105 lar approach was introduced for learning class discriminative clusters of spatial  
 106 columns [10]. However, these approaches influence the trained network and trade  
 107 accuracy for explainability, whereas ours finds meaningful inference explanations  
 108 without interfering with the network learning process.  
 109

110 **Modeling relationships between consecutive layers.** In CNNVis [11], neu-  
 111 rons in each layer are clustered to form groups having similar activity patterns.  
 112 For the clustering, a neuron was described using a  $C$ -dimensional vector of its  
 113 average activity on each class  $1, \dots, C$ . A graph between clusters of subsequent  
 114 layers was then formed based on the average weight strengths between cluster  
 115 neurons. Note that this method clusters neurons, while we cluster activity vec-  
 116 tors (of neuronal columns) across examples. Olah et al. [12] proposed a tool for  
 117 visualizing the network path for a single image. They decomposed each layer's  
 118 activations into groups using matrix factorization, and connected groups from  
 consecutive layers into a graph structure similar to [11].  
 119

## 120 3 Method

121 Inference graphs for an MLP, for which a full graphical model can be suggested,  
 122 are presented in Section 3.1. The more general case of a CNN is discussed in  
 123 Section 3.2, and its related graph-mining algorithm in Section 3.3. Models can be  
 124 trained on the full set of network layers or on a subset, indexed by  $l \in \{1, \dots, L\}$ .  
 125

### 127 3.1 Inference Graphs for MLPs

128 The hidden layer activity of an MLP network composed of FC layers can be mod-  
 129 eled by a single probabilistic graphical model with an HMM structure, enabling  
 130 closed-form inference. The model structure is shown in Fig. 2.  
 131

132 The activation vector of the  $l$ th FC layer with  $D^l$  neurons,  $x^l = (x^l[1], \dots, x^l[D^l])$   
 133  $\in \mathbb{R}^{D^l}$ , results from a mixture of  $K^l$  hidden states (i.e., clusters) with a discrete  
 134 hidden variable  $h^l \in \{1, \dots, K^l\}$  denoting the cluster index. To model the ReLU

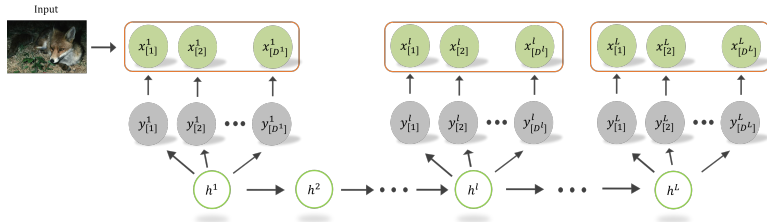


**Fig. 2. HMM for MLP networks.** Orange rectangles represent post-ReLU layer activity. Activation  $x^l[d]$  of neuron  $d$  in layer  $l$  is generated from a rectified Gaussian density, where  $x^l[d]$ 's parent,  $y^l[d]$ , is a Gaussian density before rectification, and  $h^l$  is a hidden variable generating the hidden vector of multivariate Gaussians.

operation, each activation  $x^l[d]$  is generated from a rectified Gaussian distribution [13]. The conditional probability  $P(x^l|h^l)$  is hence assumed to be a rectified multivariate Gaussian distribution with a diagonal covariance matrix. Connections between hidden variables in consecutive layers are modeled by a conditional probability table (CPT)  $P(h^l|h^{l-1})$ .

Using this generative model, an activity pattern for the network is sampled by three steps. First, a path  $(h^1, \dots, h^L)$  of hidden states is generated according to the transition probabilities  $P(h^l = k|h^{l-1} = k') = t_{k,k'}^l$ , where  $t^l \in \mathbb{R}^{K^l \times K^{l-1}}$  is a learned CPT. For notation simplicity, we define  $h^0 = \{\}$ , so  $P(h^1|h^0)$  is actually  $P(h^1)$  parametrized by  $P(h^1 = k) = t_k^1$ . After path generation, "pre-ReLU" Gaussian vectors  $(y^1, \dots, y^L)$ , with  $y^l \in \mathbb{R}^{D^l}$ , are generated based on the chosen hidden variables. A single variable  $y^l[d]$  is formed according to

$$P(y^l[d]|h^l = k) \sim \mathcal{N}(y^l[d]|\mu_{d,k}^l, \sigma_{d,k}^l), \quad (1)$$

where  $\mu_{d,k}^l$  and  $\sigma_{d,k}^l$  are the mean and standard deviation of the  $d$ th element in the  $k$ th cluster of layer  $l$ . Since the observed activity  $x^l[d]$ , generated as  $x^l[d] = \max(y^l[d], 0)$ , is a deterministic function of  $y^l[d]$ , its conditional probability  $P(x^l[d]|y^l[d])$  can be written as

$$P(x^l[d]|y^l[d]) = \begin{cases} \delta_{x^l[d]=y^l[d]}, y^l[d] > 0 \\ \delta_{x^l[d]=0}, y^l[d] \leq 0 \end{cases}, \quad (2)$$

with  $\delta_{(x=c)}$  as the Dirac delta function concentrating the distribution mass at  $c$ .

The full likelihood of the model is given by

$$P(X, Y, H|\Theta) = \prod_{l=1}^L P(h^l|h^{l-1})P(y^l|h^l)P(x^l|y^l), \quad (3)$$

where  $Y, H, X$  are tuples representing their respective variables across all layers (e.g.,  $H = \{h_l\}_{l=1}^L$ ), and the equation's components are stated above.

**Training algorithm:** In [14], the EM formulation was suggested for training a mixture of rectified Gaussians. We extended this idea to the HMM formulation

in an online setting. Following [15], the online EM algorithm tracks the sufficient statistics using running averages, and updates the model parameters using these statistics. Explicit update formulas in terms of the tracked sufficient statistics are presented in the Supplementary Material.

### 3.2 Inference Graphs for CNNs

**Layer dictionaries:** In a CNN, the activation output of the  $l$ th convolutional layer is a tensor  $X^l \in R^{H^l \times W^l \times D^l}$ , where  $H^l$ ,  $W^l$ , and  $D^l$  correspond to the height, width, and number of maps, respectively. We consider the activation tensor as consisting of  $H^l \times W^l$  spatial column examples,  $x_p^l \in R^{D^l}$ , located at  $p = (i, j) \in \{\{1, \dots, H^l\} \times \{1, \dots, W^l\}\}$ , and wish to model each such location as containing a separate visual word from a dictionary shared by all locations.

The number of hidden variables (one per location) is much larger than that in an FC layer (where a single hidden variable per layer was used), and their connectivity pattern across layers is dense, leading to a graphical model with high induced width, but with infeasible exact inference. Hence, we turn to simpler model and training techniques that are scalable to the size and complexity of CNNs. In this model, spatial column  $x_p^l$  is described as arising from a GMM of  $K^l$  clusters, regarded as visual words forming the layer dictionary. Using a training image set  $S_T = \{(I_n, y_n)\}_{n=1}^{N_T}$ , the GMM is trained independently for each layer of interest. While each location  $p$  in layer  $l$  has a separate hidden random variable,  $h_p^l$ , the GMM parameters are shared across all the spatial locations of that layer. After model training, the activity tensor of layer  $l$  for an example  $I$  can be mapped into a tensor  $P \in R^{H^l \times W^l \times K^l}$ , holding  $P(h_p^l(I) = k)$ . With slight abuse of notation, we say that  $h_p^l(I) = k^*$  (an activation column of image  $I$  in position  $p$  is assigned to cluster  $k^*$ ) iff  $k^* = \text{argmax}_k P(h_p^l(I) = k)$ . Accordingly, visual word  $k$  in layer  $l$  is the cluster  $C_k^l = \{(I, p), I \in S_T : h_p^l(I) = k\}$  containing activations over all positions for all images in the training set  $S_T$ , where cluster  $k$  has the highest  $P(h_p^l(I) = k)$ .

When the CNN also contains global layers, these can be modeled using a GMM trained on the layer's activity vectors. This can be regarded as a degenerate case of convolutional layer modeling, where the number of spatial locations is one. Specifically, the output layer of the network,  $X^L$ , containing the  $M$  class of predicted probabilities, is modeled using a GMM of  $M$  components. This GMM is not trained, and instead is fixed such that  $\mu_{d,m} = 1$  for  $d = m$  and 0 otherwise, with a constant standard deviation of  $\sigma_{d,m} = 0.1$ . In this setting, cluster  $m$  of the output layer contains images that the network predicts to be of class  $m$ .

**Probabilistic connections between layer dictionaries:** Transition probabilities between visual words in consecutive layers are modeled a-posteriori. For two consecutive modeled layers  $l$  and  $l'$  ( $l' < l$ ), the receptive field  $R(p)$  of location  $p$  in layer  $l$  is defined as the set of locations  $\{q = p + o : o \in O\}$  in layer  $l'$  used in the computation of  $x_p^l$ .  $O$  is a set of  $\{(\Delta x, \Delta y)\}$  integer offsets. Using a validation sample  $S_V = \{I_n\}_{n=1}^{N_V}$ , we compute the co-occurrence matrix

225  $N \in M^{K^l \times K^{l'}}$  between the visual words contained in the dictionaries of layers  $l$   
226 and  $l'$ ,

$$\text{227} \quad N(k, k') = |\{(I_n, p, q) : h_p^l(I_n) = k, h_q^{l'}(I_n) = k', q \in R(p)\}|. \quad (4)$$

228 Using  $N$ , we can obtain the following first and second order statistics:

$$\text{229} \quad \hat{P}(h^l = k) = \frac{\sum_j N(k, j)}{\sum_{i,j} N(i, j)} \quad (5)$$

$$\text{230} \quad \hat{P}(h_q^{l'} = k' | h_p^l = k, q \in R(p)) = \frac{N(k, k')}{\sum_j N(k, j)} = \quad (6)$$

$$\text{231} \quad \frac{|\{(I_n, p, q) : h_p^l(I_n) = k, h_q^{l'}(I_n) = k', q \in R(p)\}|}{|O| \cdot |\{(I_n, p) : h_p^l(I_n) = k\}|} = \frac{1}{|O|} \sum_{o \in O} \hat{P}(h_{p+o}^{l'} = k' | h_p^l = k).$$

232 The transition probabilities as defined above are abbreviated in the following  
233 discussion to  $\hat{P}(h^{l'} = k' | h^l = k)$ . These probabilities are averaged over spe-  
234 cific positions in the receptive field, since modeling of position-specific transition  
235 probabilities separately would lead to proliferation in the parameter number.

236 **Training algorithm:** The GMM parameters  $\Theta^l$  of layer  $l$  are trained by  
237 associating a GMM layer to each modeled layer of the network. Since we do  
238 not wish to alter the network's behavior, the GMM gradients do not propagate  
239 towards lower layers of the network. We considered two optimization approaches  
240 for training  $\Theta^l$ :

241 (1) *Generative loss* — The optimization objective is to minimize the negative  
242 log-likelihood function:

$$\text{243} \quad \mathcal{L}_G(X^l(I_n), \Theta^l) = - \sum_{p \in (H^l \times W^l)} \log \sum_{k=1}^{K^l} \pi_k^l G(x_p^l(I_n) | \mu_k^l, \Sigma_k^l), \quad (7)$$

244 where  $G$  is the Gaussian distribution function, and  $\pi_k^l$  is the mixture probability  
245 of the  $k$ 'th component in layer  $l$ .

246 (2) *Discriminative loss* — The probability tensor  $P$  is summarized into a his-  
247 togram of visual words  $Hist^l(X^l(I_n)) \in R^{K^l}$  using a global pooling operation.  
248 A linear classifier  $\mathcal{W} \cdot Hist^l(X^l(I_n))$  is formed and optimized by minimizing a  
249 cross entropy loss, where  $\mathcal{W}$  is the classifier weights vector,

$$\text{250} \quad \mathcal{L}_D(X^l(I_n), \Theta^l) = - \log P(\hat{y}_n = y_n | \mathcal{W} \cdot Hist^l(X^l(I_n), \Theta^l)), \quad (8)$$

251 and  $\hat{y}_n$  is the predicted output after a softmax transformation.

252 Comparison between these two approaches is given in Section 4.3.

253 For ImageNet-scale networks, full modeling of the entire network at once may  
254 require thousands of visual words per layer. Training such large dictionaries is  
255 not feasible with current GPU memory limitations (12GB for a TitanX). Our  
256 solution is to train a class-specific model, explaining network behavior for a spe-  
257 cific class  $m$  and its “neighboring” classes, i.e., all classes erroneously predicted  
258 by the network for images of class  $m$ . The set of neighboring classes is chosen  
259 based on the network's confusion matrix computed on the validation set. The  
260 model is trained on all training images of class  $m$  and its neighbors.

### 270    3.3 Maximum-Likelihood-Based Node Selection

271 Consider a graph in which column activity clusters (i.e., visual words)  
 272  $\{C_k^l\}_{l=1,k=1}^{L,K^l}$  are the nodes, and transition probabilities between clusters of  
 273 consecutive layers quantify edges between the nodes. Typically, this graph contains  
 274 thousands of nodes and, thus, is not feasible for human interpretation. How-  
 275 ever, specific subgraphs may have high explanatory value. Specifically, nodes  
 276 (clusters) of the final layer  $C_k^L$  in this graph represent images for which the  
 277 network predicted a class  $k$ . To understand this decision, we evaluate clusters  
 278 in the previous layer  $C_{k'}^{L-1}$  using a score based on the transition probabilities  
 279  $P(h^L = k | h^{L-1} = k')$ . The step of finding such a set of “explanatory” clusters in  
 280 layer  $L - 1$  is repeated to lower layers. Below, we develop an iterative algorithm  
 281 that using a validation subset of images  $\Omega = \{I_n\}_{n=1}^N$  outputs a subgraph of  
 282 the nodes that most “explain” the network decisions on  $\Omega$ , where “explanation”  
 283 is defined in the maximum-likelihood sense. We first explain node selection for  
 284 a single visual word in a single image, and then extend this notion to a full  
 285 algorithm operating on multiple visual words and images.

286  
 287 **Explaining a single visual word:** Consider an instance of a single visual word  
 288  $h_p^l(I) = s$ , derived from a column activity location  $p$  in layer  $l$  for image  $I$ . For  
 289 this visual word, we look for the visual words in  $R(p)$  most contributing to its  
 290 likelihood (omitting the image notation  $I$  in  $h_p^l(I)$  for brevity):

$$291 \quad P\left(h_p^l = s \mid \{h_q^{l'} : q \in R(p)\}\right) = \frac{P\left(\{h_q^{l'} : q \in R(p)\} \mid h_p^l = s\right) \cdot P(h_p^l = s)}{P\left(\{h_q^{l'} : q \in R(p)\}\right)} \quad (9)$$

$$292 \quad \approx \frac{\prod_{q \in R(p)} P(h_q^{l'} \mid h_p^l = s) \cdot P(h_p^l = s)}{\prod_{q \in R(p)} P(h_q^{l'})}.$$

293 In the last step, two simplifying assumptions were made: conditional indepen-  
 294 dence over locations in the receptive field (nominator) and independence of lo-  
 295 cations (denominator). Taking the logarithm, we decompose the expression:

$$296 \quad \underbrace{\log P(h_p^l = s)}_{\text{constant } A} + \sum_{q \in R(p)} \log \frac{P(h_q^{l'} \mid h_p^l = s)}{P(h_q^{l'})} = \quad (10)$$

$$305 \quad A + \sum_{t=1, \dots, K^{l'}} |\{q : h_q^{l'} = t, q \in R(p)\}| \log \frac{P(h_q^{l'} = t \mid h_p^l = s, q \in R(p))}{P(h_q^{l'} = t)}.$$

306 Denote  $Q_t^{l'}(I, p) = |\{q : h_q^{l'} = t, q \in R(p)\}|$  as the number of times visual  
 307 word  $t$  appears in the receptive field of location  $p$ . We look for a subset of words  
 308  $T \subset \{1, \dots, K^{l'}\}$ , which contribute the most to the likelihood of  $h_p^l = s$ . Thus,  
 309 the problem we solve is

$$310 \quad \max_T_{|T|=Z} \left\{ \sum_{t \in T} Q_t^{l'}(I, p) \log \frac{P(h_q^{l'} = t \mid h_p^l = s, q \in R(p))}{P(h_q^{l'} = t)} \right\}, \quad (11)$$

**Algorithm 1** Inference graph building

**Input:** CNN  $CN$ , a set  $\Omega$  of validation images predicted by  $CN$  to class  $m$ ,  $Z$  nodes per layer, network model  $\{\Theta^l, \hat{P}(h^l = k), \hat{P}(h^l = k|h^{l'} = k')\}_{l=1, k=1, k'=1}^{L, K^l, K^{l'}}$   
**Output:** An inference graph  $G = (N, E)$ , where  $N$  and  $E$  hold clusters (nodes) and their weighted connections (edges) in the graph, respectively

**Initialization:** Push  $\Omega$  through the network model to get  $\{Q_{t,s}^l(\Omega)\}_{l=1}^{L-1}$  (Eq. 15) and clusters  $\{C_i^l\}_{l=1, i=1}^{L, K^l}$ . Set  $S = m$ ,  $N = C_m^L$ , and  $E = \emptyset$

For  $l = L - 1, \dots, 1$

For  $t = 1, \dots, K^l$ , compute  $S^l(\Omega, S, t)$  (Eq. 16)

Choose  $(z_1^l, \dots, z_Z^l)$  to be the  $Z$  clusters indices with the largest scores  $S^l(\Omega, S, t)$

Set  $S = (z_1^l, \dots, z_Z^l)$  and  $e_{i,j}^l = S^l(\Omega, z_i^{l+1}, z_j^l)$ ,  $\forall i, j = 1, \dots, Z$

Set  $N = N \cup \{C_{z_i^l}^l\}_{i=1}^Z$  and  $E = E \cup \{e_{i,j}^l\}_{i=1, j=1}^{Z, Z}$  // nodes and edges update

by choosing the first  $Z$  words for which the explanatory score term

$$S'(I, s, t) = Q_t^{l'}(I, p) \log \frac{P(h_q^{l'} = t | h_p^l = s, q \in R(p))}{P(h_q^{l'} = t)} \quad (12)$$

is the highest. Intuitively, the score of the  $t$ th visual word is the product of two terms,  $Q_t^{l'}(I, p)$ , which measures the word frequency in the receptive field, and  $\log \frac{P(h_q^{l'} = t | h_p^l = s, q \in R(p))}{P(h_q^{l'} = t)}$ , which measures how likely it is to see word  $t$  in the receptive field compared to seeing it in general. To compute the probabilities in the log term of the score, we use the estimations  $\hat{P}(h^l = k)$  and  $\hat{P}(h^{l'} = k'|h^l = k)$  made using Eqs. 5 and 6, respectively.

**Explaining multiple words and images:** The optimization problem presented in Eq. 11 can be extended to multiple visual words in multiple images using column position and image independence assumptions. Assume a set of validation images  $\Omega$  is being analyzed, and a set of words  $S \subset \{1, \dots, K^l\}$  from layer  $l$  has to be explained by lower layer words for these images. We would like to maximize the likelihood of the set of all column activities  $\{h_p^l(I_n) : h_p^l \in S, I_n \in \Omega\}$ , in which a word from  $S$  appears. Assuming column position independence, this likelihood decomposes into terms similar to Eq. 9:

$$\begin{aligned} \log P\left(\{h_p^l(I_n) : h_p^l(I_n) \in S, I_n \in \Omega\} \mid \{h_q^{l'}(I_n) : I_n \in \Omega\}\right) = \\ \sum_{n=1}^N \sum_{s \in S} \sum_{\{p : h_p^l(I_n) = s\}} \log P(h_p^l(I_n) | h_q^{l'}(I_n), q \in R(p)). \end{aligned} \quad (13)$$

Repeating the derivation also given in Eqs. 9, 10, and 11 for this expression, we get a similar optimization problem,

$$\max_T_{|T|=Z} \left\{ \sum_{t \in T} \sum_{s \in S} Q_{t,s}^l(\Omega) \log \frac{P(h_q^{l'} = t | h_p^l = s, q \in R(p))}{P(h_q^{l'} = t)} \right\}, \quad (14)$$

360 where  $Q_{t,s}^{l'}(\Omega)$  is the aggregation of  $Q_t^{l'}(I, p)$  over multiple positions and images  
 361

$$362 Q_{t,s}^{l'}(\Omega) = \sum_{n=1}^N \sum_{\{p: h_p^l(I_n) = s\}} Q_t^{l'}(I_n, p). \quad (15)$$

$$363$$

$$364$$

365 That is,  $Q_{t,s}^{l'}(\Omega)$  is the number of occurrences of word  $s$  with word  $t$  in its  
 366 receptive field in all the images in  $\Omega$ . The solution is given by choosing the  $Z$   
 367 words in layer  $l'$  for which the score  
 368

$$369 S^{l'}(\Omega, S, t) = \sum_{s \in S} Q_{t,s}^{l'}(\Omega) \log \frac{P(h_q^{l'} = t | h_p^l = s, q \in R(p))}{P(h_q^{l'} = t)} \quad (16)$$

$$370$$

$$371$$

$$372$$

373 is maximized. The inference graph is generated by going over the layers from the  
 374 top layer—for which the decision has to be explained—and downwards, selecting  
 375 the explaining nodes using the score of Eq. 16. See Algorithm 1 for details.  
 376

## 377 4 Results

$$378$$

$$379$$

380 Fully connected networks were trained on the MNIST [16] and CIFAR10 [17]  
 381 datasets, containing 10 classes each. The networks include six layers with the  
 382 first five containing 1,000 neurons each. Based on a preliminary evaluation, the  
 383 number of visual words  $K^l$  was set at 40 for all layers.

384 CNN models included ResNet20 [2] trained on CIFAR10, and VGG-16 [18]  
 385 and ResNet50 [2] trained on the ILSVRC 2012 dataset [19]. For ResNet20, the  
 386 output of add-layers after each skip connection were modeled, as these outputs  
 387 are expected to contain aggregated information. For ResNet50, the output of  
 388 add-layers 1, 3, 7, 13, and 16 were modeled. For VGG-16, the first convolutional  
 389 layers at each block were modeled (five layers in total). The numbers of  
 390 visual words were set at 60, 100, 200, 450, and 1,500 for Layers 1-5, respectively,  
 391 according to the GPU memory limitation.

392 In all experiments and modeled layers, the GMM’s mean parameters were  
 393 initialized using  $K^l$  randomly selected examples. The variance parameters were  
 394 initialized as the variances computed from 1,000 random examples. Prior prob-  
 395 abilities were uniformly initialized to be  $\frac{1}{K^l}$ .

### 397 4.1 MLP Inference Path

$$398$$

399 In MLP networks, the entire layer activity is assigned to a single cluster. To  
 400 visualize such a cluster, we consider it as a “decision junction”, where a decision  
 401 regarding the consecutive layer cluster is made. For this visualization, the ac-  
 402 tivity vectors in the  $C_k^l$  cluster are labeled according to their consecutive layer  
 403 clusters, forming subclusters for this cluster. We use linear discriminant analysis  
 404 (LDA) [20] to find a 2D projection of the activity vectors that maximize the

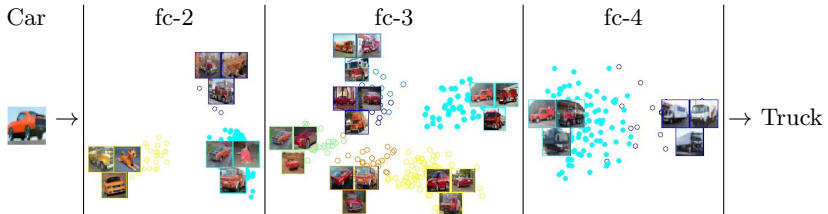


**Fig. 3. MLP inference path.** Three main decision junctions of a misclassified example in a 6-layer network. Subclusters are visualized by the three most representative examples. Points from the subcluster chosen by this example are marked by full circles.

separation of the examples with respect to their subcluster labels. Each subcluster is visualized using the three examples with the minimal  $l_2$  distance to the subcluster center.

The inference path for an example  $I$  is defined to be the maximum a-posteriori (MAP) cluster sequence, i.e.,  $H = (h^1, \dots, h^L)$ , satisfying

$$\max_{h^1, \dots, h^L} \log P(h^1, \dots, h^L | X(I)), \quad (17)$$

where  $H$  can be found using the Viterbi algorithm [21].

Such inference paths are useful for error diagnosis. In Fig. 3, a partial path containing three decision junctions of an erroneous ‘‘car’’ example in the CIFAR10 network is presented. It can be seen that the example’s likely ‘‘decisions’’ in layer fc-3 leads to car and truck clusters in the consecutive layer. At this point, due to its unconventional rear appearance, resembling a truck front, this car example was wrongly associated with a ‘‘truck’’ subcluster, an association that remained until the classification layer.

## 4.2 Cluster Similarity Across Layers

A plausible assumption about deep network representations is that early representations are input dominated, while representations in late layers are more class-related. This phenomena can be observed in our framework by considering how distance between clusters changes as a function of layer index. In Fig. 4 (left), cluster similarity matrices are presented. Each matrix shows Euclidean distances between centers of the clusters from a single layer. Clusters are ordered by their dominant class index, defined as the class whose examples are the most frequent in the cluster. For an MLP network, presented in Fig. 4 (top left), the progression toward class-related representation is evident from the emerging block structure in Layers 3-5, indicating increasing similarity between clusters representing the same class.

In contrast, as seen in Fig. 4 (bottom left), CNN clusters (representing column activities) stay local and diverse, even at the uppermost layers where their receptive fields cover the entire input space. This phenomenon is demonstrated

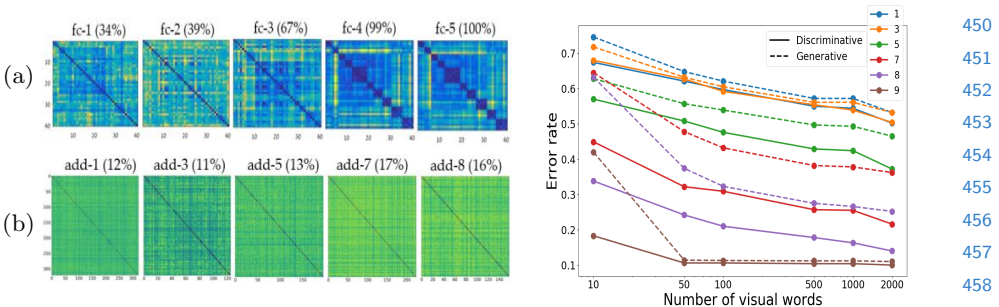


**Fig. 4. Left:** Cluster similarity matrices for increasing layer indices in a 6-layer MLP (a) and ResNet20 (b) both trained on CIFAR10. The average percentage of dominant class examples (across clusters) is stated above each matrix. **Right:** Error rates of a linear classifier trained over word histograms taken from six ResNet20 conv-layers (1, 3, 5, 7, 8, and 9) trained with either a generative or discriminative loss (Section 3.2).

by the lack of block structure, as well as the relatively low frequency of the dominant class in a cluster. This indicates that the final CNN classification is based on several class-specific words, which are not similar, and appear simultaneously in different image regions.

### 4.3 CNN Inference Graphs

**Loss and dictionary size.** Fig. 4 (right) shows the errors obtained for linear classification using dictionary histograms (Eq. 8), as a function of dictionary size. Graphs are shown for dictionaries obtained using losses  $\mathcal{L}_G$  (7) and  $\mathcal{L}_D$  (8), for several intermediate convolutional layers of the CIFAR10 network. For all layers, except the final one (indexed 9), larger dictionaries provide better classification. However, for the final layer, dictionaries larger than 50 clusters do not increase accuracy, which approaches the original network error of 0.088. As expected, the discriminative loss  $\mathcal{L}_D$  leads to smaller errors than the generatively-optimized loss. Therefore, all models presented below were trained with the  $\mathcal{L}_D$  loss.

**Class inference graph.** An example of a class inference graph for the class “pineapple” in VGG-16 is presented in Fig. 5. The graph shows that the most influential words in the top convolution layer can be roughly characterized as “grassy head” (left word), “pineapple body” (middle), and “body textured with (lower) round edge”. The origin of these words can be traced back to lower layers. For example, “grassy head” is composed of words capturing mostly “vegetation” in the layer below, which are in turn generated from words describing green texture and multiple diagonal lines (middle layer, left and middle words). Similarly, the origin of “pineapple body” can be traced back to texture words in lower layers and until the green edge filters in Layer 1.

**Image inference graphs.** Fig. 6 shows an image inference graph for a pineapple image wrongly classified to the “swing” class. Using the inference graph, we can analyze the dominant (representative) visual words that have

## Class pineapple

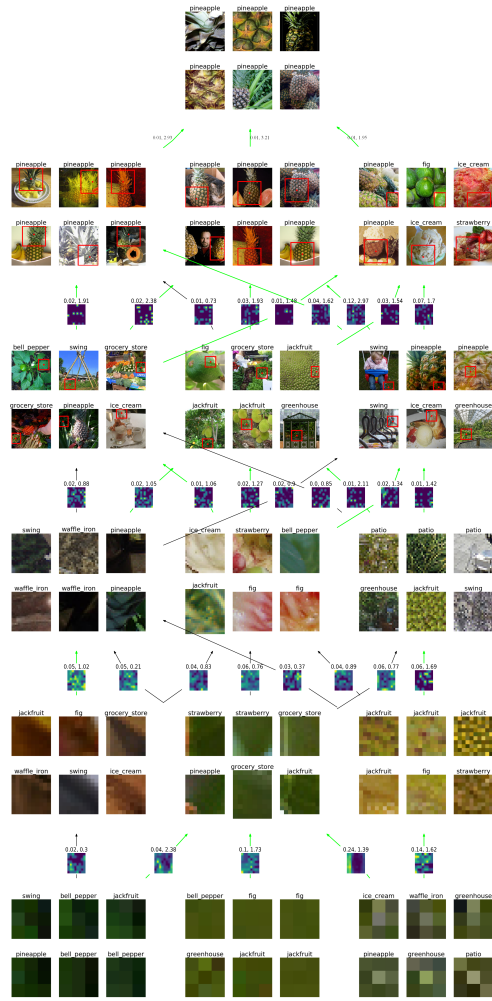


**Fig. 5. Pineapple inference graph.** The graph is generated by training a model on "pineapple" class and its neighboring classes. The top node is a visual word of the output layer, representing the predicted class "pineapple". The lower levels in the graph show the three most influential words in preceding modeled layers. Visual words are manifested by the six representative examples for which  $P(h^l = k|x_p^l)$  is the highest. For the two highest layers, examples are presented by showing the example image with a rectangle highlighting the receptive field of the word's location. For lower layers, the receptive field patches themselves are shown. Images are annotated by their true label. Arrows are shown when the log-ratio term is positive, colored green for significant connections in which the term is higher than 1. They are annotated by the frequency of the lower word in the receptive field (left) and the log ratio (right) (the two components of the score in Eq. 16). In addition, for each arrow, a heatmap is shown indicating the frequent locations of the lower-level visual words in the receptive field of the higher-level word. The figure is best inspected by zooming in on clusters of interest.

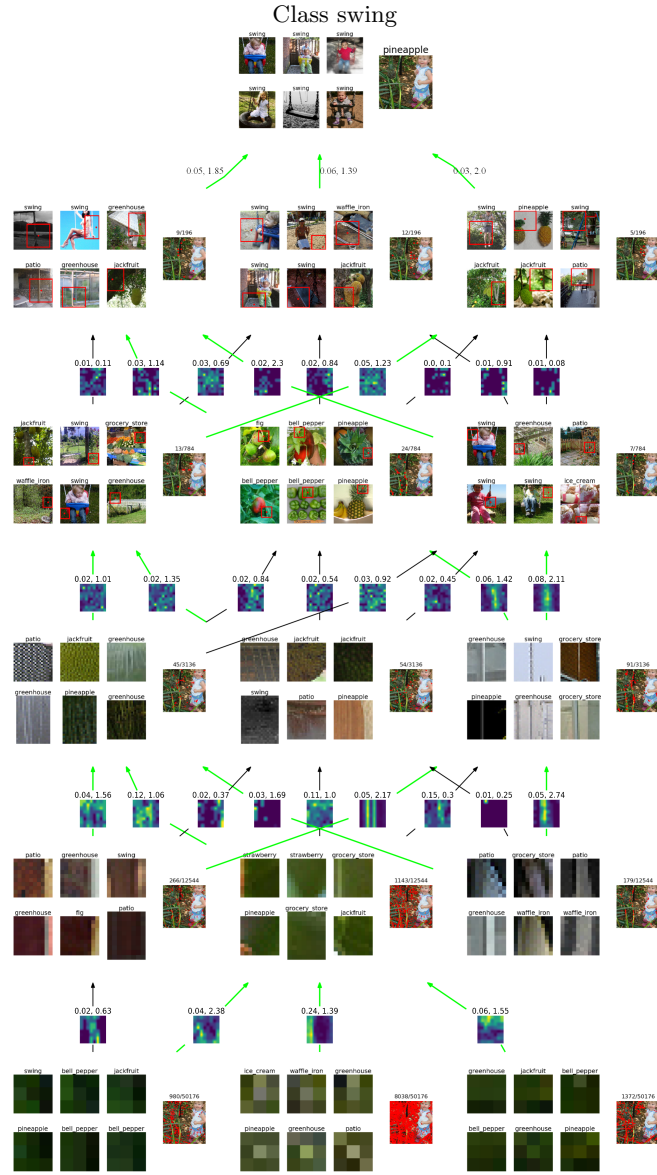


**Fig. 6. An image inference graph of an erroneous image.** An image inference graph for a pineapple image wrongly classified to the class "swing". The model is generated using "pineapple" and its neighboring classes (same as in Fig 5), where the neighbor class "swing" is included. The graph is generated by applying the node selection algorithm (Section 3.3) to a set  $\Omega$  containing this single erroneous image. The analyzed image is shown on the right side of each cluster node, with red dots marking spatial locations assigned to the cluster. The fraction of spatial examples belonging to the cluster (in this image) appears in the title.



**Fig. 7. Subgraph of the same image as in Fig. 6 classified by ResNet50.** A visual word in layer add-13 (left), leading to a visual word in layer add-16 (middle), and to correct classification of the pineapple (right).

led to this erroneous classification: **(1)** Top layer (Layer 5): The visual words voting for the swing class focus on strong vertical rope-like shapes (left), sand texture (middle), and grass/foliage texture (right). **(2)** Layers 4 and 3: The strong vertical line (left of Layer 5) originates from a similar visual word of Layer 4 (right), and this in turn depends strongly on the "isolated-vertical-line" word in Layer 3 (right). The foliage word (right in Layer 5) mainly originates from the vegetation left word in Layer 4, which in turn heavily depends on the two green "vertical-stripe-structure" words in Layer 3 (left and middle). **(3)** Layers 2 and 1: the main explanatory words in Layer 2 are green and dark vertical edges and lines, which are combined to construct the "isolated-vertical-line" word in Layer 3 (right) and the "vertical-stripe-structure" word in Layer 3 (left). These in turn are created from earlier "green-edge" words in Layer 1.

In Fig. 7, we show a partial inference graph of the same "pineapple" image wrongly classified to class "swing" by VGG-16 (Fig. 6), which is successfully classified by ResNet50. As can be seen in the top layer of the graph (add-16, middle), Resnet50 successfully detects the pineapple location in the image, where both visual words presented contain strong "pineapple" features. Additional examples of class and image inference graphs are given in the Supplementary Material.

## 5 Conclusion

We introduced a new approach for interpreting hidden layers activity of deep neural networks by learning dictionaries of activity clusters and transition probabilities between clusters of consecutive modeled layers. We formalized a maximum-likelihood criterion for mining clusters relevant for network prediction, which enable building explanatory inference graphs of manageable size. Inference graphs can be constructed for an entire classes, to understand the general network reasoning for this class, or for specific images, for which error analysis may specifically be sought. The tools developed can be used to verify the soundness of the network reasoning and to understand its hidden inference mechanisms, or conversely to reveal network weaknesses. The code for the framework algorithms is available at <https://bit.ly/38pcatH>.

## 630 References

- 631 1. Krizhevsky, A., Sutskever, I., Hinton, G.E.: ImageNet classification with deep  
632 convolutional neural networks. In: Advances in Neural Information Processing  
633 Systems. (2012) 1097–1105
- 634 2. He, K., Zhang, X., Ren, S., Sun, J.: Deep residual learning for image recognition. In:  
635 Proceedings of the IEEE Conference on Computer Vision and Pattern Recognition.  
636 (2016) 770–778
- 637 3. Huang, G., Liu, Z., Van Der Maaten, L., Weinberger, K.Q.: Densely connected  
638 convolutional networks. In: Proceedings of the IEEE Conference on Computer  
639 Vision and Pattern Recognition. (2017) 4700–4708
- 640 4. Erhan, D., Bengio, Y., Courville, A., Vincent, P.: Visualizing higher-layer features  
641 of a deep network. University of Montreal **1341**(3) (2009) 1
- 642 5. Simonyan, K., Vedaldi, A., Zisserman, A.: Deep inside convolutional net-  
643 works: Visualising image classification models and saliency maps. arXiv preprint  
644 arXiv:1312.6034 (2013)
- 645 6. Yosinski, J., Clune, J., Nguyen, A.M., Fuchs, T., Lipson, H.: Understanding neural  
646 networks through deep visualization. CoRR **abs/1506.06579** (2015)
- 647 7. Zhou, B., Khosla, A., Lapedriza, A., Oliva, A., Torralba, A.: Learning deep fea-  
648 tures for discriminative localization. In: Proceedings of the IEEE Conference on  
649 Computer Vision and Pattern Recognition. (2016) 2921–2929
- 650 8. Zeiler, M.D., Fergus, R.: Visualizing and understanding convolutional networks.  
651 In: European Conference on Computer Vision, Springer (2014) 818–833
- 652 9. Liao, R., Schwing, A., Zemel, R., Urtasun, R.: Learning deep parsimonious repre-  
653 sentations. In: Advances in Neural Information Processing Systems. (2016) 5076–  
654 5084
- 655 10. Chen, C., Li, O., Tao, D., Barnett, A., Rudin, C., Su, J.K.: This looks like that: deep  
656 learning for interpretable image recognition. In: Advances in Neural Information  
657 Processing Systems. (2019) 8928–8939
- 658 11. Liu, M., Shi, J., Li, Z., Li, C., Zhu, J., Liu, S.: Towards better analysis of deep  
659 convolutional neural networks. IEEE Transactions on Visualization and Computer  
660 Graphics **23**(1) (2016) 91–100
- 661 12. Olah, C., Satyanarayan, A., Johnson, I., Carter, S., Schubert, L., Ye, K., Mordv-  
662 intsev, A.: The building blocks of interpretability. Distill **3**(3) (2018) e10
- 663 13. Soccia, N.D., Lee, D.D., Seung, H.S.: The rectified Gaussian distribution. In:  
664 Advances in Neural Information Processing Systems. (1998) 350–356
- 665 14. Lee, G., Scott, C.: EM algorithms for multivariate Gaussian mixture models with  
666 truncated and censored data. Computational Statistics & Data Analysis **56**(9)  
667 (2012)
- 668 15. Cappé, O., Moulines, E.: On-line Expectation–Maximization algorithm for latent  
669 data models. Journal of the Royal Statistical Society: Series B (Statistical Method-  
670 ology) **71**(3) (2009) 593–613
- 671 16. LeCun, Y., Cortes, C., Burges, C.: MNIST handwritten digit database. AT&T  
672 Labs [Online]. Available: <http://yann.lecun.com/exdb/mnist> **2** (2010)
- 673 17. Krizhevsky, A., Hinton, G., et al.: Learning multiple layers of features from tiny  
674 images. Technical report, University of Toronto (2009)
- 675 18. Simonyan, K., Zisserman, A.: Very deep convolutional networks for large-scale  
676 image recognition. arXiv preprint arXiv:1409.1556 (2014)
- 677 19. Russakovsky, O., Deng, J., Su, H., Krause, J., Satheesh, S., Ma, S., Huang, Z.,  
678 Karpathy, A., Khosla, A., Bernstein, M., Berg, A.C., Fei-Fei, L.: ImageNet large

675 scale visual recognition challenge. International Journal of Computer Vision **115**(3) 675  
676 (2015) 211–252 676

677 20. Fukunaga, K.: Introduction to statistical pattern recognition. Academic Press 677  
678 (1990) 678

679 21. Forney, G.D.: The Viterbi algorithm. Proceedings of the IEEE **61**(3) (1973) 268– 679  
680 278 680

681

682

683

684

685

686

687

688

689

690

691

692

693

694

695

696

697

698

699

700

701

702

703

704

705

706

707

708

709

710

711

712

713

714

715

716

717

718

719

675

676

677

678

679

680

681

682

683

684

685

686

687

688

689

690

691

692

693

694

695

696

697

698

699

700

701

702

703

704

705

706

707

708

709

710

711

712

713

714

715

716

717

718

719